



ELSEVIER

Available online at www.sciencedirect.com

SCIENCE @ DIRECT®

Earth and Planetary Science Letters 236 (2005) 120–134

EPSL

www.elsevier.com/locate/epsl

Mode of crustal extension determined by rheological layering

Chris Wijns^{a,b,*}, Roberto Weinberg^{c,2}, Klaus Gessner^{b,1}, Louis Moresi^{d,3}

^a*School of Earth and Geographical Sciences, University of Western Australia, Crawley, WA 6009, Australia*

^b*CSIRO Exploration and Mining, PO Box 1130, Bentley, WA 6102, Australia*

^c*School of Geosciences, Monash University, Building 28, VIC 3800, Australia*

^d*School of Mathematical Sciences, Monash University, Building 28, VIC 3800, Australia*

Received 12 April 2004; received in revised form 17 May 2005; accepted 28 May 2005

Available online 28 June 2005

Editor: R.D. van der Hilst

Abstract

The results of numerical modelling show that the mechanical stratification of the crust provides the fundamental control on fault spacing and, ultimately, the mode of extension. Macroscopic pre-existing structures and weaknesses are often thought to govern the behaviour of continental crust under extension, and many prior studies have focussed on the effect of heterogeneities in triggering faulting and exhumation of lower crustal material. The role played by such features is in fact subordinate to that exerted by the rheological contrast from upper to lower crust. In our numerical model, the temperature gradient dictates the transition from a strong, brittle, upper crust to a weaker, ductile, lower crust. We see two distinct extension modes that depend on this vertical rheological contrast: the *distributed faulting mode* and the *metamorphic core complex mode*. The ratio of the integrated strength of the upper to lower crust is an indicator of the resulting mode of extension. When this strength ratio is small, i.e., the lower crust is relatively strong, the result is distributed, densely spaced faulting, with limited slip on each fault, and no exposure of lower crustal rocks. An example could be faulting in the North Sea. A large strength ratio, hence a weak lower crust that flows easily, leads to stretching being strongly localised onto relatively few normal fault zones. Each fault accommodates large displacements, eventually dissecting the upper crust and resulting in exhumation of the lower crust. This is representative of the metamorphic core complexes of the western U.S.A. and the Aegean. The actual critical strength ratio for the transition between modes will depend upon secondary factors such as the relative thickness of the lower crust with respect to the upper crust and the degree of fault weakening.

© 2005 Elsevier B.V. All rights reserved.

Keywords: fault spacing; rheology; metamorphic core complex; continental extension

* Corresponding author. School of Earth and Geographical Sciences, University of Western Australia, Crawley, WA 6009, Australia. Tel.: +61 8 9261 6125; fax: +61 8 6488 1178.

E-mail addresses: chris.wijns@csiro.au (C. Wijns), roberto.weinberg@sci.monash.edu.au (R. Weinberg), klaus.gessner@csiro.au (K. Gessner), louis.moresi@sci.monash.edu.au (L. Moresi).

¹ Tel.: +61 8 6436 8627.

² Tel.: +61 3 9905 4902.

³ Tel.: +61 3 9905 4468.

1. Introduction

Continental lithosphere may be highly extended without entirely rifting to a new ocean basin. For example, total Cenozoic strain estimates (β factors) of up to 2 have been proposed for parts of the Basin and Range in the western U.S.A., which has not been rifted (e.g., [1,2]). A total of up to 80% extension ($\beta=1.8$) is suggested on a very large scale of 300–500 km [3], and Niemi et al. [4] have even suggested 500% extension in central Death Valley, California, since the middle Miocene. Stretching of the crust may then be accommodated by two contrasting phenomena: distributed, closely spaced and limited-slip normal faulting over a large area, or localised, large-strain normal faulting that often results in the complete dissection of the upper crust and exhumation of the lower crust. Examples of distributed faulting exist in the North Sea, e.g., the Gullfaks area near Bergen, Norway [5] and the Danish basin [6], where faults are characterised by a relatively steep angle and small offset. Normal faults that exhibit a low angle and very large displacement, juxtaposing exhumed high-grade metamorphic rocks against near-surface rocks, are the hallmarks of a metamorphic core complex (MCC), as in the Basin and Range (e.g., [7–10]) or the Aegean (e.g., [11–14]).

Why should extending lithosphere sometimes form an MCC in preference to failing in a distributed manner? One possibility is that major lateral discontinuities in the strength of either the upper crust (e.g., pre-existing faults) or the lower crust (e.g., partial melt zones) focus stresses and localise extension. Christiansen and Pollard [15] have documented field evidence for the nucleation of shear zones from pre-existing dikes acting as weaknesses, although these were not associated with an MCC. In their conceptual models of extensional tectonics, both Wernicke [16] and Wernicke and Axen [17] assume an immediately active horizontal or low-angle detachment surface through the upper crust, which then controls faulting and exhumation of the lower crust. In some analogue modelling experiments, initial faults end up controlling fault spacing and the mode of extension (e.g., [18]). Brun et al. [19] conclude that a weak rheological zone at the base of the upper crust, such as a magma body, is required to trigger an MCC. Other analogue modellers (e.g., [20,21]) employ a pre-weak-

ened lower lithosphere to localise stresses and influence the resulting extension, and Corti et al. [21] add an imposed basal velocity discontinuity to this. Some numerical modelling experiments also suppose initial weaknesses and proceed to investigate related factors that vary the results of extension (e.g., [22]). Although such weak features do serve to focus stresses, we find that in the absence of lateral heterogeneities, vertical contrasts in rheology dictate whether one or the other mode of extension will result. In fact, small lateral heterogeneities are often insufficient to trigger an MCC mode when the rheological layering promotes distributed faulting.

The mode of extension is determined by the combined ability of both lateral and vertical rheological structure to focus stresses in the brittle upper crust. Our numerical modelling concentrates on the role of the vertical rheological contrast in dictating the spacing between fault zones and the accompanying mode of distributed faulting or MCC formation. Numerical models have the advantage over analogue experiments of exact control over “laboratory” conditions, and precise specification of rheological behaviour and initial and boundary conditions. On the other hand, given the level of readily available computational power today, numerical models still lack the resolution of analogue models, especially in three dimensions. Thus, we confine ourselves to 2D vertical section simulations, which, fortunately, are easily compared to much published analogue modelling, including that of Brun et al. [19].

2. Models

We use a two-dimensional Lagrangian integration point finite-element code [23,24] to explore the different behaviours of the crust during extension. The algorithm solves the governing equations of momentum, mass, and heat conservation. Inertial terms are neglected in the momentum equation

$$\sigma_{ij,j} + \rho g_i = 0$$

in which σ_{ij} is the Cauchy stress, ρ is the density, and g_i is the gravitational force. The incompressibility condition

$$v_{i,i} = 0$$

holds for velocities v_i , and heat conservation without internal sources follows

$$\frac{dT}{dt} - \kappa T_{,ii} = 0$$

for the material derivative of temperature T and thermal diffusivity κ . The time step is decided implicitly by a Courant condition on the maximum velocity within the model and effected via a finite-difference formulation.

The particle-in-cell continuum approach allows simulations to develop very large strains comparable to those found in analogue models, while still tracking strain history accurately for the constitutive laws. Examples of geological and engineering problems are in Moresi and Lenardic [25] and Mühlhaus et al. [26,27].

We consider a viscoplastic crust with strain weakening behaviour, which gives rise to the localisation of deformation and necking of layers. A plastic yield law approximates brittle behaviour below a critical temperature, which governs a transition from upper crust to purely ductile lower crust. The initial geometry of the model (Fig. 1) corresponds to the thicknesses used by Brun et al. [19]: 20 km of upper crust atop 40 km of lower crust, along a length of 160 km. Horizontal and vertical stripes are simply marker materials to enhance visualisation (as in Brun et al. [19]). Above these two crustal layers is a highly compressible layer of low-viscosity, low-density, background material (“air”), which does not interfere with the mechanics of the problem. All walls of the closed bounding box are free-slip and vertical walls have zero heat flux. Neglecting the upper mantle in this simplified Earth model, in

conjunction with the free-slip lower boundary, forcibly implies a crustal system effectively decoupled from the lower lithosphere. This would be the case for a sufficiently mobile lower crust. We note, however, that, in the distributed faulting mode, the free-slip lower boundary does not exert any influence different from a zero-slip boundary, as will be seen below. Extension proceeds by applying a uniform velocity to the right-hand boundary, equivalent to 100% strain in 5 Ma, or 6.3×10^{-15} /s, as determined in the field work of Gessner et al. [14] for the Menderes metamorphic core complex in western Turkey. This boundary velocity is low enough to not create tensional stresses, so gravity is in effect driving the deformation.

The yield law for the upper crust prescribes a maximum shear stress τ_{yield} , calculated via the second invariant of the deviatoric stress tensor. This simple criterion is not an implementation of Coulomb plasticity, i.e., there is no dilation angle.

$$\tau_{\text{yield}} = (c_o + c_p p) f(\epsilon_p) \quad (1)$$

where p is the pressure, c_o is the cohesion, or yield stress at zero pressure, and c_p is the pressure dependence of the yield stress, equivalent to the friction coefficient in Byerlee’s law [28]. A low rock cohesion of 16 MPa ([29], p. 155) is greater than the value of zero employed in Byerlee’s law for the upper 10 km of the crust, but avoids a cohesionless surface material that would allow plastic strain along the entire air–rock interface. Numerous laboratory experiments by Byerlee [28] resulted in a universal friction coefficient of 0.6–0.85 for most rock types. However, this is for dry samples. Assuming an average hydrostatic pore pressure, the solid pressure is reduced by more than one

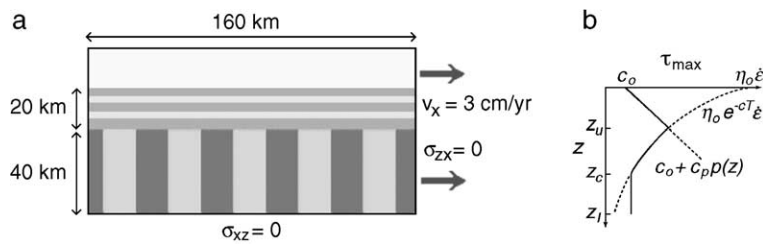


Fig. 1. (a) Initial geometry and boundary conditions for the numerical model. Stripes in the upper and lower crust are marker materials for visualising deformation. All subsequent simulation results are represented at this same scale. (b) Representative maximum shear stress profile (solid line) through the crust for a given strain rate $\dot{\epsilon}$. Neglecting localised strain weakening, strength increases with pressure p from c_o at the surface to a maximum value at the base z_u of the brittle upper crust, at which point the yield curve intersects the viscous, temperature-dependent flow law. To avoid any extremely low viscosity, the value at some depth z_c is adopted as a minimum value and is constant to the base z_1 of the crust.

third, so that an equivalent dry friction coefficient of 0.7 is reduced to 0.44 in our model. This translates into a maximum shear strength of about 250 MPa at the brittle to ductile transition. Strain weakening is included through the empirical power law function $f(\varepsilon_p)$, in which ε_p is the accumulated plastic strain, measured as the second invariant of the deviatoric plastic strain tensor:

$$f(\varepsilon) = \begin{cases} 1 - a(\varepsilon_p/\varepsilon_0) & \varepsilon_p < \varepsilon_0 \\ 1 - a & \varepsilon_p \geq \varepsilon_0 \end{cases}$$

No further weakening takes place beyond the “saturation” strain ε_0 , at which point the yield stress has been reduced by a proportion a . Both of these parameters are varied in order to investigate the influence of fault weakening on the mode of extension.

A fixed density contrast defines a boundary between upper and lower crustal material, although the mechanical behaviour of all material depends solely on the temperature, as explained below. Initially, the density contrast corresponds to the depth at which the temperature dictates a change from brittle to ductile behaviour. While in reality this density contrast should probably be deeper within the rocks of the lower crust, the final conclusion is that density differences barely affect the simulation results. The ductile behaviour of the lower crust is Newtonian, as we are concentrating on the effects of strength contrasts without recourse to complicated rheologies. With increasing extension, the lower crust may be exhumed into the brittle field and undergo faulting. It behaves mechanically as the upper crust does, but retains its original density (i.e., metamorphic grade and mineralogy). We do not consider any thermal expansion, which has a minor buoyancy effect compared to compositional density contrasts; nor do we model melting.

Viscosity η varies with temperature T according to the Frank-Kamenetskii relation ([30], Chapter 6, pp. 340–341)

$$\eta(T) = \eta_0 e^{-cT}. \quad (2)$$

This is a simplification of an Arrhenius rheology, where the constants η_0 and c are chosen such that the viscosity at the interface z_u between upper and lower crust, which is the initial brittle to ductile transition, satisfies the maximum yield stress

$$\tau_{\text{yield}}(z_u) = \eta(T(z_u))\dot{\varepsilon}$$

i.e., the maximum shear stress profile through the crust is continuous. The mechanical transition from brittle to ductile behaviour is always at the intersection of the yield curve and the viscous flow law (Fig. 1b). Appendix B contains a full development of this relation. To avoid an extremely low viscosity at the base of the crust z_1 , we limit $\eta(T) > \eta(T_c)$ for some maximum temperature T_c . The constants used in Eq. (2) are arbitrarily chosen to construct physically realistic viscosity profiles and not to reflect physical measures. The result is a maximum viscosity variation of two orders of magnitude from the top of the lower crust to the point of minimum viscosity. In our constant velocity extension model, the crustal strength profile (Fig. 1b) evolves with a changing strain rate, but provides a convenient starting point from which to characterise the crust.

The surface of the upper crust is maintained at 0 °C. Since the temperature scale can be chosen independently of other variables, we fix this only for comparison with field data in a later section. For reference, an initial temperature gradient of 17.5 °C/km results in a brittle to ductile transition at 350 °C, in the range discussed by Brace and Kohlstedt [31] and references therein, and McKenzie and Fairhead [32]. This transition temperature also corresponds to theoretical flow laws derived by Handy et al. [33] for various crustal components.

Table 1 contains parameter values for the natural system, which apply to all simulations unless explicitly stated otherwise. The scaling equations that

Table 1
Natural parameter values

Parameter	Value
Depth z_u , upper crust	20 km
Depth z_1 , lower crust	60 km
Velocity U , boundary	3.1 cm/yr
Strain rate $\dot{\varepsilon}$, initial	$6.3 \times 10^{-15}/\text{s}$
Density ρ_u , upper crust	2700 kg/m ³
Density ρ_l , lower crust	3000 kg/m ³
Gravity g	10 m/s ²
Cohesion c_0	16 MPa
Friction coefficient c_p	0.44
Strain weakening a	0.8 (0.2, simulation D)
“Saturation” strain ε_0	0.5 (1.0, simulation D)
Thermal diffusivity κ	10^{-6} m ² /s
Temperature T_s , surface	0 °C

Parameters a and ε_0 are modified for simulation D as indicated.

translate these into model values are in Appendix A. Values for the viscosity law (2) are not listed because they change with every simulation, but the discussion section offers some natural viscosity equivalents.

3. Results

In all of the following simulations, bands of high localised plastic strain are proxies for fault zones in the continuum code. Accumulated plastic strain in the brittle crust is indicated by darkened material, and the degree of shading is a measure of this accumulation. Unless otherwise noted, a maximum of 80% strain weakening ($a=0.8$) occurs after an accumulated plastic strain $\varepsilon_o=0.5$. These values reflect evidence, from both numerical experiments (e.g., [34]) and field-based heat-flow measurements (e.g., [35,36]), that major faults may undergo significant weakening.

The different behaviours of the crust under extension are partly parameterised by the ratio r_τ of integrated upper to lower crustal strength. Appendix C contains the calculation of integrated strengths, based on the maximum sustainable shear stress at a given strain rate.

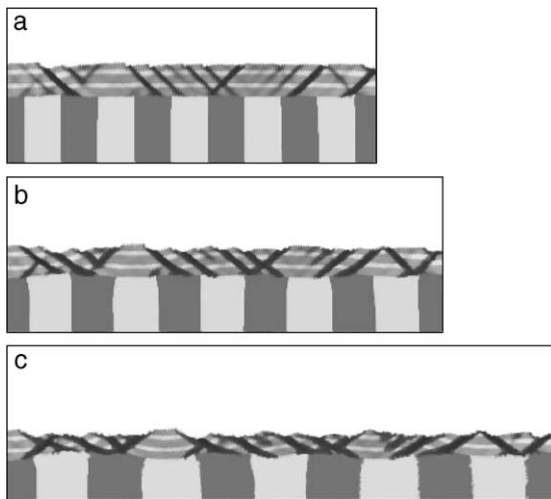


Fig. 2. Simulation A: evolution of distributed faulting mode with a lower crust of constant viscosity and $r_\tau=0.53$. Total extension of (a) 24% (1.2 Ma), (b) 52% (2.6 Ma) and (c) 82% or 130 km (4.1 Ma). Dark bands in the upper crust indicate accumulated plastic strain or fault zones.

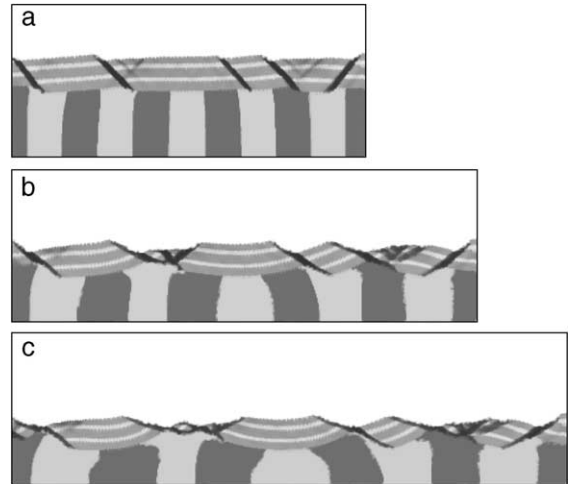


Fig. 3. Simulation B: evolution of MCC mode caused by a uniformly weak lower crust of constant viscosity and $r_\tau=2.52$. Total extension of (a) 25% (1.2 Ma), (b) 53% (2.7 Ma) and (c) 83% (4.2 Ma).

3.1. Constant viscosity

The two contrasting modes of crustal extension are first illustrated for a constant viscosity lower crust (Figs. 2 and 3), for comparison with the results of Brun et al. [19]. In these cases, the continuous viscosity profile, described above, does not apply, but the yield curve does govern the upper crust rheology. When the system is characterised by a small $r_\tau=0.53$ (i.e., relatively high viscosity lower crust), the result is distributed faulting (simulation A, Fig. 2). The upper crust develops many closely spaced steep faults, each of which accommodates limited strain, and the interface between upper and lower crust remains relatively flat. This result is very similar to the tilted block mode of Brun et al. [19], although, according to the information supplied, $r_\tau \approx 1.8$ for their analogue model. This discrepancy is probably due in large part to differences in material properties for the experiments and is addressed later in the discussion. Even with more than 80% extension ($\beta > 1.8$), the upper crust in simulation A is never completely dissected. New steep faults form soon after older faults have accommodated a small amount of shear strain, breaking the upper crust into a series of small blocks that undergo limited rotation.

Although Brun et al. [19] propose that a weakness is needed in the lower crust in order to localise stresses and trigger an MCC mode of extension, we

show in simulation B (Fig. 3) that a uniformly weak lower crust (high $r_\tau = 2.52$) is sufficient to achieve this behaviour. Deformation is accommodated by only a few normal fault zones. Displacement is large within each fault zone, which, through fault weakening, remains active even after rotating to a shallow dip. The lower crust flows easily to isostatically compensate for localised thinning of the upper crust, which enhances block rotation and continued strain on low-angle faults. Despite the Newtonian rheology of the lower crust, strain is localised as a result of kinematic interaction with the plastic (non-Newtonian) upper crust. The lower crust is first exhumed at $\beta = 1.6$.

The fault patterns in both simulations above are dynamic: although the first faults that develop remain to the end, they do not continue to accommodate strain if they have rotated to a shallow enough angle. This is true to the theory of Andersonian faulting. The empirical strain-softening law for the crust allows fault zones to remain active until a low angle, but further displacement takes place on new, steep faults. During distributed faulting, the large number of active faults pre-empts significant rotation of any one of them and the initial fault pattern is relatively stable. In MCC mode, rotation of early faults leads to an evolving pattern with the addition of later faults.

3.2. Temperature-dependent viscosity

The main limitation in using a constant viscosity for the lower crust, and therefore a limitation of the analogue modelling, is that lower crustal material that rises towards the surface remains very weak, although it should cool and strengthen, even becoming brittle. This phenomenon does not affect the case of distributed faulting, where the lower crust remains buried below a laterally stable brittle to ductile transition (Fig. 2). In fact, the simulation result for a distributed faulting mode with a temperature-dependent viscosity profile is entirely similar to that for a constant viscosity lower crust. In MCC mode, however, exhumation and cooling will influence the tectonics.

A weak lower crust with a temperature-dependent rheology, in a laterally uniform system, gives rise to the MCC mode in Fig. 4. The rising lower crust enters the brittle domain, but cooling is slow enough,

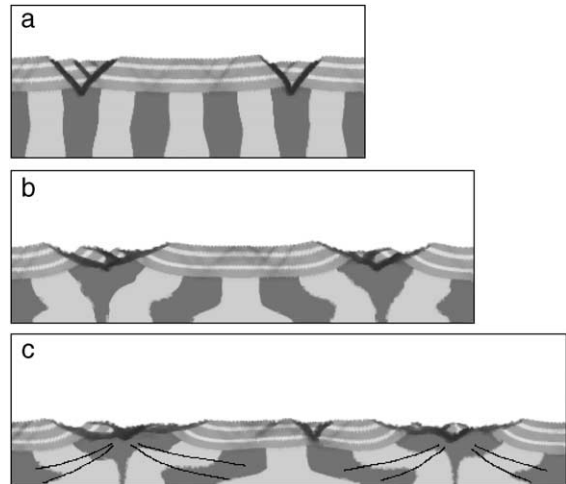


Fig. 4. Simulation C: evolution of MCC mode ($r_\tau = 2.15$) with both a viscosity and a brittle to ductile transition that are temperature-dependent. Total extension of (a) 16% (0.8 Ma), (b) 53% (2.6 Ma) and (c) 82% (4.1 Ma). Faults continue to propagate through the newly brittle lower crust as it nears the surface and are connected to diffuse high shear zones in the ductile region, indicated with pairs of solid lines in (c).

relative to exhumation, that brittle deformation of the lower crust does not penetrate to great depth. The propagation of faults from the upper crust into the exhuming lower crust allows continued strain along the original structures, until they become very gently dipping or even flat-lying detachment surfaces accommodating large displacements. There is evidence in the vertical lower crust markers that these faults are spatially connected to diffuse high shear zones that extend to the base of the entire crust. These deep shear zones are traced in Fig. 4c and show much greater localisation than in the case of constant viscosity (Fig. 3). Such brittle fault to ductile shear continuity has been suggested in an intraplate setting by Zoback et al. [37].

Despite a decrease in r_τ relative to the constant viscosity MCC of simulation B, fewer fault zones exist in simulation C. The greater tendency to MCC mode is due to the variable viscosity profile that, although higher in an integrated sense, allows much lower viscosity material near the base of the model to dominate crustal flow and tectonic expression. This is apparent when comparing the strain visualisation markers in the lower crust (Figs. 3c and 4c).

In order to determine the importance of fault weakness with respect to MCC formation, simulation D

(Fig. 5) has a maximum strain weakening of only 20% ($a=0.2$) instead of 80% as in simulation C, and this weakening accumulates more slowly through $\varepsilon_0=1.0$ instead of 0.5. The resulting extension still produces an MCC mode, although the characteristics are different. Fault zones are more numerous and more diffuse, and the upper crust tends to neck rather than produce planar shear zones. Although these stronger fault zones initially evolve as for the case of simulation C, they are less effective in accommodating continued strain, so higher inter-fault stresses develop, causing new faults to form.

3.3. Field validation

We test the physical validity of the MCC simulation C by comparing our numerical results with cooling data from the Kuzey detachment in the Central Menderes. After 100% extension, the crust is approximately 30 km thick, in agreement with a seismic interpretation of western Turkey by Saunders et al. [38]. Both field and numerical temperature–time curves for exhumed footwall material are similar (Fig. 6a). The field data, from Gessner et al. [14] and Hetzel et al. [39], reflect measurements from apatite and zircon fission-track thermochronology, and $^{40}\text{Ar}/^{39}\text{Ar}$ ages for the higher temperatures. Temperature in the numerical model is scaled to match the initial 300 °C of the exhumed field sample. The numerical curve does not reach the surface temperature of 0 °C because, due to the continuum nature of the code, the upper crust is never completely removed from above the exhumed lower crust, so that the lower crust remains marginally buried and begins to stabilise at approximately 75 °C.

The match between cooling rates for the numerical and field data suggests that the model formulation provides an adequate physical description for our investigation of extensional tectonics. Parsons et al. [40] provide observations that could further argue the



Fig. 5. Simulation D: MCC mode with $r_\tau=2.15$, but a maximum fault weakening of 20% rather than 80% as in simulation C. Total extension of 80% (4.0 Ma).

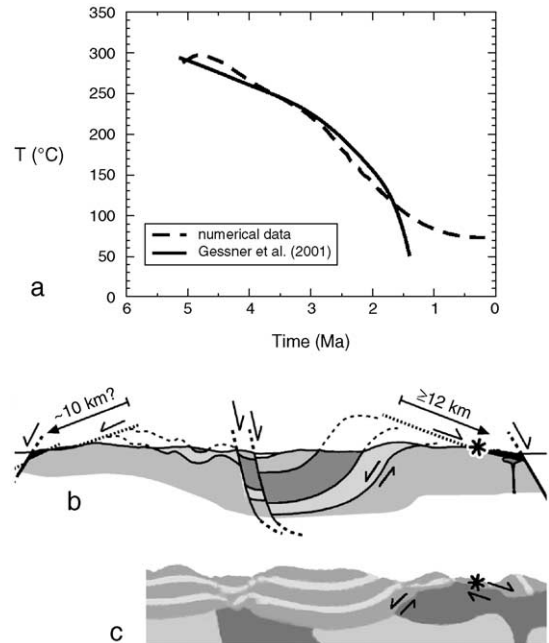


Fig. 6. (a) Temperature–time paths for an exhumed footwall of an MCC from fission-track thermochronology and $^{40}\text{Ar}/^{39}\text{Ar}$ ages (from Gessner et al. [14]) and from numerical simulation C. The numerical data are scaled to match the 300 °C initial field temperature. (b) Schematic cross section of Central Menderes MCC from Gessner et al. [14]. The asterisk denotes the location, in high-grade metamorphic material, of the laboratory analyses. (c) Part of simulation C with an asterisk showing the final location of the numerical temperature sampling point.

case for weak lower crust promoting MCC formation. They note that a low seismic velocity middle crust (hotter and/or weaker) is present under the Buckskin-Rawhide core complex in Arizona, U.S.A. Further west, Parsons et al. [40] observe that the middle crust has a high velocity (colder and/or stronger) under the steep normal faults of the Salton Trough.

4. Discussion

4.1. Continuum between modes

Pre-existing faults or thermal and rheological heterogeneities are not required to produce an MCC mode of extension. A large ratio of upper to lower crustal strength is necessary, often overcoming distributed initial faults. As the ratio r_τ is further increased, we reach a state where a single fault is nucleated and

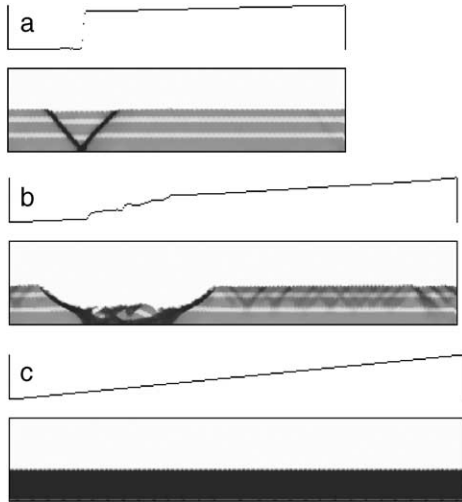


Fig. 7. (a) Endmember of MCC mode ($r_\tau \rightarrow \infty$) represented by the brittle upper crust over a free-slip lower boundary. Total extension of 3% (0.15 Ma). The profile above is the normalised basal velocity. (b) Same simulation as (a) at a total extension of 38% (1.9 Ma). Because of the continuum nature of the code, there is some stress transmitted across the graben. At this stage, gravitational slumping also begins to affect the simulation because there is no lower crust isostatic compensation. (c) Endmember of distributed faulting mode ($r_\tau \rightarrow 0$) represented by the brittle upper crust over a no-slip boundary. Total extension of 40% (2.0 Ma).

remains the only zone of failure. This is illustrated by the endmember case $r_\tau \rightarrow \infty$ of a single brittle layer extended over a free-slip lower boundary (Fig. 7a and b), which is the limit of very weak lower crust that effectively decouples the upper crust from the tectonics below. Once a fault or symmetric graben is nucleated, boundary stresses can no longer be communicated laterally through the layer and the velocity gradient approaches zero away from the fault, as apparent in the basal velocity profile plotted above the section. If the fault was truly a discontinuity (impossible with this continuum code), the velocity gradient would be zero everywhere except at the discontinuity, unlike the profile in Fig. 7b, where some stress continues to be transmitted. The lower crust, when present, fulfills the role of stress distributor and ensures non-zero traction at the base of the brittle crust. For the hypothetical case of a lower crust that is so strong as to maintain a constant stress at this interface, $r_\tau \rightarrow 0$ and a zero-slip basal condition exists (Fig. 7c). The resulting uniform yield of the upper crust is the endmember of distributed faulting.

The $r_\tau \rightarrow \infty$ case in Fig. 7b will not necessarily result in MCC formation. The presence of a volume of mobile lower crust may be essential for block rotation, shallowing of fault dips and lower crust exhumation. Fault zone localisation and significant block rotation are complementary expressions of the weak lower crust endmember. These two phenomena might not be separable in nature.

Simulations A to C, together with the endmember cases in Fig. 7, suggest that the number of major fault zones that develop to accommodate extension correlates inversely with the tendency towards MCC mode. This is borne out in Fig. 8, in which the number of faults and mode of extension are plotted against the strength ratio of the crust r_τ . Faults are counted if they transect the upper crust and graben are counted as one fault zone. To illustrate, in Fig. 7b, only one fault zone is present. The trend is that fewer fault zones develop with increasing r_τ . More simulations have been run than are shown in the previous section, in order to

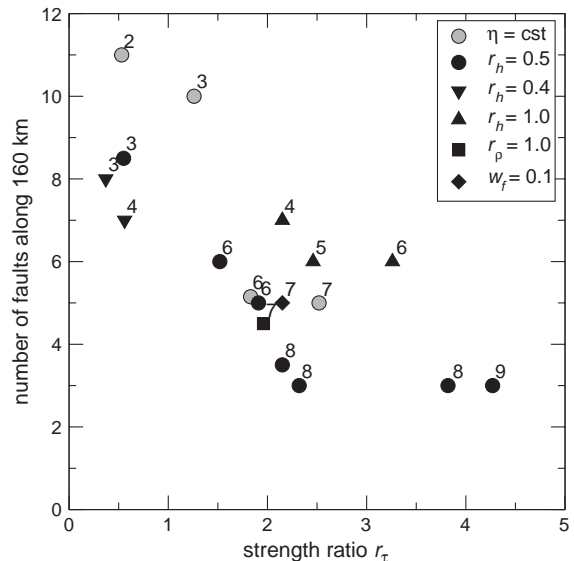


Fig. 8. Number of major fault zones as a function of r_τ . Data labels indicate an evaluation of the model result between the distributed endmember (0) and the MCC endmember (10). Unless otherwise indicated, the standard simulations (filled circles) have a temperature-dependent lower crust viscosity, thickness ratio $r_h = 0.5$, density ratio $r_\rho = 0.9$, and fault weakness factor $w_f = 0.53$. The total crustal thickness is 56 km for $r_h = 0.4$ and 40 km for $r_h = 1.0$. While r_τ controls the overall trend, changes in the other variables, especially r_h , move results vertically for equal r_τ and horizontally for equal mode or number of faults.

explore the phase space of extension modes. Results are labelled with a subjective rank from 0 to 10, corresponding to position between the endmembers of, respectively, distributed faulting and MCC mode. In addition to r_τ , the following parameters simplify the classification of results: the ratio $r_h = z_u/z_1$ of upper to lower crust thickness, the ratio r_ρ of upper to lower crust density, and the fault weakness factor $w_f = a/(1 + \varepsilon_0)$. A larger w_f implies greater and/or more rapid fault weakening. According to Fig. 8, variations in r_τ exert the greatest control on the mode of extension. Of secondary but significant importance is r_h , while r_ρ and w_f have a minor influence. The extension rate in these simulations may be too high for density contrasts to appreciably affect exhumation of the lower crust. Buoyancy forces will be more evident for lower extension rates, at some point dictating a transition to diapirism for $r_\rho > 1$.

To explain why strength contrasts may control the mode of extension, we turn to analytic work by Montési and Zuber [41] that explains fault spacing in a layered lithosphere based on the preferred wavelengths from an instability analysis. The observations on our numerical simulations are that:

- (1) at the onset of extension, many faults are nucleated in both modes.
- (2) when r_τ is small, many of the nascent fault zones are activated.
- (3) when r_τ is large, few fault zones are activated.

For a brittle layer with localising properties above a viscous substrate, Montési and Zuber [41] calculate the perturbation wavenumber with the highest growth rate. This relates directly to our observations above, where certain wavelengths of fault spacing are activated out of numerous initial perturbations (fault nuclei). Montési and Zuber [41] determine that a lower substrate viscosity results in a smaller dominant wavenumber (their Figs. 7, 10 and 13); hence, a longer wavelength of fault spacing in the brittle layer, just as in our numerical results. The emergence of a dominant wavelength is controlled by resonances within the localising (upper) layer.

Some further insight into the physical controls behind the dependence of fault spacing on substrate viscosity may be derived from numerical experiments by Bai and Pollard [42]. For a fractured layer sand-

wiched between two unfractured layers, Bai and Pollard [42] find that there is a critical fracture spacing to layer thickness below which the interfracture stress is always compressive and new fractures will not form. At greater fracture spacings, the stress becomes tensile and eventually overcomes the tensile strength of the layer, leading to new infill fractures. This critical spacing to thickness ratio increases with increasing ratio of Young's modulus between the fractured and neighbouring layers. With the caveat that the Bai and Pollard [42] analysis is for linear elastic media and deals with tensile fracturing, we find an exact analogue in our results for normal faulting of viscoplastic layers. As the strength ratio r_τ increases, the spacing between active faults increases. This suggests that the magnitude of lateral stress transfer from the unfaulted lower crust to the upper crust may be a key to the mode of extension, where the mode is specifically controlled by the number of active fault zones. A relatively strong lower crust provides greater traction at the base of the upper crust, which results in the yield stress being reached at shorter spacings between faults. The existence of few fault zones in the presence of a weak lower crust is simultaneously linked to the ability of crustal blocks to rotate because of lower crustal mobility, leading to MCC formation.

The effect of crustal thickness ratios is more straightforward. For equal values of the integrated upper crustal strength, a thicker upper crust (greater r_h) simply requires more strain until it is dissected. Montési and Zuber [41] conclude the same dependence between fault spacing and brittle layer thickness. However, because it is restricted to an infinitely deep substratum, the theory of Montési and Zuber [41] cannot explain the effect of a thin lower crust. A thin lower crust (greater r_h) relies largely on lateral flow to compensate for unloading, and thus, at the same integrated viscosity as a thick lower crust, does not accommodate an MCC mode of extension as easily. For a sufficiently thin lower crust, the simple relation between fault spacing and brittle layer thickness will break down.

When the different thickness ratios r_h are accounted for, the standard deviation of model behaviour is largely reduced. Fig. 9 shows the more or less direct variation between normalised fault spacing and r_τ/r_h for the temperature-dependent simulations with $r_\rho = 0.9$ and $w_f = 0.53$. The greatest fault spacing

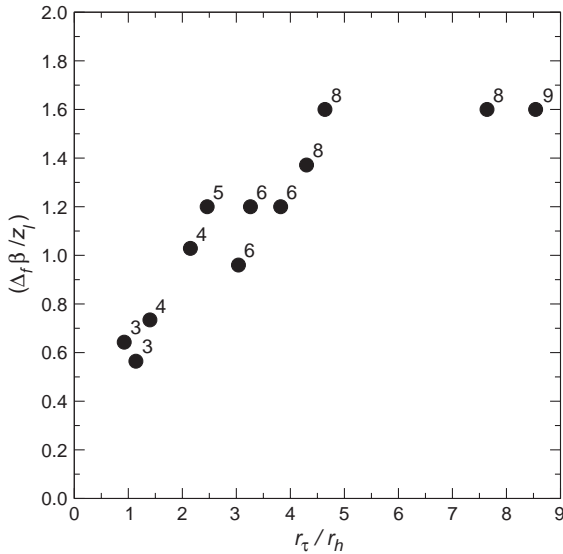


Fig. 9. Spacing Δ_f of major fault zones (normalised by final crustal thickness z_1/β) as a function of r_τ/r_h for temperature-dependent simulations with $r_\rho=0.9$ and $w_f=0.53$. Data labels indicate the mode as in Fig. 8. The trend should pass through the origin (cf. Fig. 7c for $r_\tau/r_h \rightarrow 0$) and towards infinite spacing for $r_\tau/r_h \rightarrow \infty$, although these cases would not be reached for natural parameter ranges for the crust.

achieved with our model setup is about 1.6 times the total crustal thickness. The deviation from the trend for the two simulations with highest r_τ/r_h is most likely due to boundary conditions, i.e., the box is finite and there will always be at least one fault during the experiment.

With respect to fault weakening, our results are consistent with those of Montési and Zuber [41]. The stronger faults in simulation D reflect the condition in Montési and Zuber [41] where the effective stress exponent dictates less efficient localisation and more prevalence of the necking mode. This is well illustrated in Fig. 5. We note that Montési and Zuber [41] also find, as we do, that density contrasts relevant to Earth conditions have little effect on fault spacing.

The simplistic empirical prediction of fault spacing and extension mode in Fig. 9 might be difficult to relate to field observations in a quantitative sense, i.e., through measurements of upper and lower crustal thickness, β factor, etc. Seismic data would be needed to differentiate between and measure the depth intervals of upper and lower crust. Previous studies have related fault spacing to the effective elastic thickness

T_e of the lithosphere (e.g., [43]), where the relationship first established by Vening-Meinesz [44], in studying graben formation, is that greater T_e leads to increased fault spacing. This takes marginal account of the ductile lower crust, because T_e is a measure of the elastic/brittle components of the entire lithosphere and is likely dominated by the depth extent of a strong upper mantle. Restricting comparison to the two-layered Earth we consider, a larger T_e would reflect a greater proportion of upper to lower crust, in which case this study is in agreement with the work of Ebinger and Hayward [43]. A true analysis of T_e (including a strong upper mantle) versus fault spacing is outside the scope of this study.

Other physical formulations for the model would likely change the absolute values of our defining parameters, but we have shown that there exists a continuum of behaviour in extension that depends mostly upon the contrast between upper and lower crustal strength, modulated by crustal thickness ratios. Furthermore, after significant extension ($\beta > 1.8$), we have found only two endmember modes. A small r_τ results in a contiguous upper crust even after extreme stretching, whereas a large r_τ initiates more localised strain that evolves into an MCC.

4.2. Comparison with other modelling and with nature

As suggested earlier, the value of $r_\tau=1.8$ for the distributed faulting mode of Brun et al. [19] should lead to an intermediate mode of extension, according to our numerical results. The thicker lower crust ($r_h=0.33$) in Brun et al. [19] would push the model even further into the MCC field (cf. Fig. 9). A sand upper crust (not viscoplastic), less extension, periodic extension due to the experimental set-up, and insufficient basal lubrication may all be factors, which preclude meaningful comparison between these numerical and analogue results.

Our model does not incorporate upper mantle, which limits direct comparison with the modes of extension of Buck [45]. However, an equivalent “narrow rift” mode in our simulations is simply a juvenile MCC mode in terms of total extension. Strain is localised in one or few zones, but the lower crust is not yet exhumed. Analogue modelling by Benes and Davy [46] purports to uphold the modes of Buck [45],

in which they use a similar measure of layer strength ratios as we do to distinguish model behaviour. They conclude that very weak lower crust gives rise to an MCC mode of extension, and our results are broadly consistent with theirs. While Benes and Davy [46] also classify a narrow rift mode, they change the upper to lower crust thickness ratio with respect to their core complex simulations to achieve this. A narrow rift, which they classify after only 9.3% extension, is the result of a thicker upper crust and a thinner lower crust, which both contribute to hindering exhumation of the lower crust. We suspect that given greater extension, the narrow rifts of Benes and Davy [46] are actually core complexes, whereas the “wide rifts” will remain as such, equivalent to our distributed faulting results. Narrow rifts are an intermediate mode and not an endmember behaviour.

The upper mantle will have some influence on the behaviour of the crust during extension. The thinner or stronger the lower crust, the more likely this influence will manifest itself. The lower crust in our simulations is sufficiently thick and ductile that it effectively decouples the crust from the upper mantle. If the upper mantle is strong, it will then remain relatively flat, as the lower crust will flow more quickly than the mantle in response to any unloading. This case is implicit in our use of a rigid, zero-traction bottom boundary, and corresponds to the observations of a flat Moho boundary under areas of high extension in Arizona [47]. On the other hand, if the upper mantle is of comparable viscosity to the lower crust, it will participate in isostatic compensation. In our present model, this would be equivalent to increasing the thickness of the lower crust. Although the upper mantle may be involved in the long-term support of surface loads during crustal deformation [2], our study points out that the viscosity of the lower crust is largely responsible for the rapid establishment of fault spacing after the onset of extension, which is a phenomenon on a different time scale.

The geometric origin of low-angle detachment faults remains controversial. According to Scott and Lister [48] and Livaccari et al. [49], for example, structural field relations favour initiation and activation at a shallow dip. Others such as Buck [50] and Wernicke and Axen [17] propose initial high-angle faults that subsequently rotate to shallow dip. In all of our simulations, initial high-angle normal faults form

as planar features that evolve to shallower angles because of lower crustal flow, or isostatic compensation, during unloading of the footwall. The faults are not listric but initially dip at approximately 45° due to the nature of the implemented rheology. We expect that listric faults would enhance block rotation, so that our trend from distributed faulting to MCC mode will be moved towards lower values of r_τ in systems of listric faults. The rotation of high-angle faults first manifests itself at the base of the upper crust, where the changes in the local stress field are greatest. Continued unroofing and lower crustal flow can eventually produce very shallow faults such as those of Fig. 4c. These results do not contradict the hypothesis that detachment faults are formed at low angle. There is simply no condition present for an initial stress field rotated from the vertical, and new faults form at a specific angle to σ_1 . However, the results do illustrate and support the hypothesis that initial high-angle faults can rotate to low angle and develop into shallow detachment faults that continue to slip due to significant weakening.

It is worth noting a Coulomb failure analysis by Wills and Buck [51] that determines the likelihood of fault slip at shallow dips due to specific boundary or loading conditions. They conclude that slip will not occur on low-angle surfaces unless there exists a questionable combination of localised, near-lithostatic pore pressure and unsustainably high tensile stresses in the upper 5 km of the crust. On the other hand, if normal faults form at shallow dips because of pre-existing weaknesses, for example earlier shallow thrust faults (e.g., [52]), such structures can alter the stress field and also override the control of vertical rheological strength contrasts on fault spacing.

Through numerical experiments on a single elastoplastic layer, Lavier et al. [53] find that both the layer thickness and the amount of fault weakening can affect the degree of offset per fault. However, because the Lavier et al. [53] experiments are over an inviscid substrate, they nucleate a single fault zone only (this includes a single graben or horst with secondary faults in the same zone), i.e., the endmember of MCC mode (Fig. 7a). They achieve fault rotation by allowing influx of filler material from the base. By including the important role of the lower crust in distributing stresses, we have determined fault weakening to be

less important than the rheological contrast between upper and lower layers of the crust.

A more sophisticated model by Lavier and Buck [54] includes a visco-elastic lower crust. While their purpose is to investigate the influence of cooling rate on faulting style, their results fit within our description of modes. Our estimated values of r_τ for the simulations presented by Lavier and Buck [54] are all very high, such that they are well within an MCC mode and consequently nucleate single fault zones, albeit sometimes composed of more than one individual fault.

Finally, we translate r_τ values into natural viscosity for the lower crust and compare with independent estimates. It is difficult to express the integrated viscosity as a single value, since the profile varies considerably with depth. Observational estimates based on, for example, post-glacial rebound or post-seismic relaxation of crustal velocities are probably reflective of the most mobile part of the lower crust. We therefore use the minimum viscosity of the lower crust (below z_c) to crudely compare results. The distributed faulting mode with $r_\tau=0.53$ has a lower crust viscosity of 10^{22} Pa s. The MCC mode in simulation C returns a viscosity of 4.5×10^{20} Pa s. We have no estimates of lower crustal viscosity for western Turkey, but in the western U.S.A., Pollitz et al. [55] calculate an upper limit of 5×10^{20} Pa s based on geodetic measurements of post-seismic velocity fields after the 1999 Hector Mine earthquake in California. This value is very close to the model value for the MCC mode, but the distributed mode viscosity appears very high. For a better comparison with the western U.S.A., we modify the initial lower crust thickness to 20 km ($r_h=1$), which, after extension, leaves a total crustal thickness of between 20 and 25 km, consistent with the regional crustal thickness model of Chulick and Mooney [56] for the Basin and Range. Now the distributed faulting mode occurs for a viscosity of 6×10^{21} Pa s and the MCC mode for a viscosity of 2.5×10^{20} Pa s or lower.

5. Conclusion

The primary rheological control on the mode of extension in the Earth's crust is the ratio of upper to lower crustal strength. This ratio dictates fault spacing

in the upper crust through the stress transfer from ductile lower crust to brittle upper crust. This fault spacing, naturally linked to the ability of the lower crust to flow, controls the subsequent evolution of the normal fault systems. Although pre-existing weaknesses could be responsible for the initiation of many large detachment faults and metamorphic core complexes, a true mode of extension, which does not rely on large-magnitude initial heterogeneities to control fault spacing, is the result of vertical rheological contrasts. A small ratio of upper to lower crustal strength leads to a distributed mode of faulting, where many faults take up limited strain, and the upper crust is never completely pulled apart. A large strength ratio results in few active fault zones, each accommodating a large amount of strain. This leads to block rotation and complete dissection of the upper crust, with the consequent exhumation of lower crustal rocks. Examples of this mode of extension may be the metamorphic core complexes of the western U.S.A. and the Aegean. The actual critical strength ratio for the transition between modes will depend upon such factors as the relative thickness of the lower crust with respect to the upper crust, and the degree of fault weakening. These are secondary factors that do not alter the primary importance of vertical rheological contrasts in determining the mode of extension.

Acknowledgements

Dr. Laurent Montesi and one anonymous reviewer provided references and criticisms that improved the discussion of physical insight and related studies.

Appendix A. Scaling

The following scaling factors are the ratio of natural to model parameter values and contain the appropriate SI units. The model bounding box initially measures one dimensionless unit in height by two units in length and represents a true system 160 km long. Comparison of natural versus model dimensions leads to a length scale

$$L^* = \frac{L_{\text{nature}}}{L_{\text{model}}} = 8 \times 10^4 \text{ m.}$$

A model boundary velocity of 1.0 translates into a strain rate of 0.5. The true strain rate of $6.3 \times 10^{-15}/\text{s}$ results in a scale factor $\dot{\epsilon}^* = 1.26 \times 10^{-14}/\text{s}$.

Equivalence of lithostatic versus viscous stresses demands that

$$\sigma^* = \rho^* g^* L^* = \eta^* \dot{\epsilon}^*.$$

Both the gravitational and density scales g^* and ρ^* are equal to unity, so the resultant viscosity scale $\eta^* = 6.35 \times 10^{18}$ Pa s.

Matching the Peclet number $Pe = \dot{\epsilon} L^2 / \kappa$ for both systems, with a natural thermal diffusivity $\kappa = 10^{-6}$ m², yields $\kappa^* = 8 \times 10^{-5}$ m².

Appendix B. Viscosity at brittle to ductile transition

In order to create a continuous maximum shear stress profile as in Fig. 1b, the viscosity η_u at the brittle to ductile transition z_u must satisfy both the brittle yield Eq. (1) and the temperature-dependent viscosity Eq. (2).

$$\eta_u = \frac{\tau_{\text{yield}}(z_u)}{\dot{\epsilon}} = \eta_o e^{-cT(z_u)}.$$

Having fixed c_o and c_p , η_u is derived from Eq. (1) for the yield stress before any strain softening, noting that the total overburden pressure p is the lithostatic stress reduced by the tensional stress.

$$c_o + c_p(\rho_u g z_u - \eta_u \dot{\epsilon}) = \eta_u \dot{\epsilon}$$

$$\eta_u = \frac{c_o + \rho_u g z_u c_p}{(1 + c_p) \dot{\epsilon}}.$$

With the parameter values from Table 1, the transition viscosity $\eta_u = 2.75 \times 10^{22}$ Pa s. The constants η_o and c control the viscosity profile through the ductile region and are related through the equations above.

$$e^{-cT(z_u)} = \frac{\eta_u}{\eta_o}$$

$$c = -\frac{1}{T(z_u)} \ln \left(\frac{c_o + \rho_u g z_u c_p}{(1 + c_p) \eta_o \dot{\epsilon}} \right).$$

Appendix C. Integrated crustal strength

Referring to Fig. 1b, the integrated strength τ_{int} of the crust is simply the area between 0 and the max-

imum shear stress. This maximum stress is defined by the yield envelope in the brittle zone (Eq. (1)) and by the viscous stress $\eta \dot{\epsilon}$ in the ductile zone. The crustal response to extension is defined by the ratio r_τ of the integrated strength of the upper crust (initially all brittle) to that of the lower crust (initially all ductile):

$$r_\tau = \frac{\tau_{u(\text{int})}}{\tau_{l(\text{int})}}.$$

For the upper crust at the onset of extension,

$$\begin{aligned} \tau_{u(\text{int})} &= \int_0^{z_u} \tau_{\text{yield}} dz \\ &= c_o z_u + \frac{1}{2} z_u (\tau_{\text{yield}}(z_u) - c_o) \\ &= c_o z_u + \frac{1}{2} z_u \left(\frac{c_o + \rho g z_u c_p}{1 + c_p} - c_o \right) \\ &= \frac{z_u}{2} \left(c_o + \frac{c_o + \rho g z_u c_p}{1 + c_p} \right). \end{aligned}$$

Integrating the viscous stress profile for the lower crust at an initial constant strain rate and linear temperature profile,

$$\begin{aligned} \tau_{l(\text{int})} &= \int_{z_u}^{z_1} \eta(T) \dot{\epsilon} dz \\ &= \dot{\epsilon} \int_{z_u}^{z_1} \eta_o e^{-cT} dz \\ &= \dot{\epsilon} \int_{z_u}^{z_c} \eta_o e^{-c \frac{\partial T}{\partial z} dz} + \dot{\epsilon} \int_{z_c}^{z_1} \eta_o e^{-cT(z_c)} dz \\ &= -\frac{\eta_o \dot{\epsilon}}{c \frac{\partial T}{\partial z}} \left[e^{-c \frac{\partial T}{\partial z} z} \right]_{z_u}^{z_c} + \eta_o \dot{\epsilon} e^{-cT(z_c)} (z_1 - z_c) \\ &= -\frac{\eta_o \dot{\epsilon}}{c \frac{\partial T}{\partial z}} \left[e^{-cT(z_c)} - e^{-cT(z_u)} \right] \\ &\quad + \eta_o \dot{\epsilon} e^{-cT(z_c)} (z_1 - z_c). \end{aligned}$$

References

- [1] A. Lachenbruch, J. Sass, Models of extending lithosphere and heat flow in the Basin and Range province, in: R. Smith, G. Eaton (Eds.), *Cenozoic Tectonics and Regional Geophysics of the Western Cordillera*, Mem.-Geol. Soc. Am., vol. 152, Geological Society of America, Boulder, Colorado, 1978, pp. 209–250.
- [2] C. Jones, B. Wernicke, G. Farmer, J. Walker, D. Coleman, L. McKenna, F. Perry, Variations across and along a major

- continental rift: an interdisciplinary study of the Basin and Range province, western USA, *Tectonophysics* 213 (1992) 57–96.
- [3] B. Wernicke, J. Spencer, B. Burchfiel, P. Guth, Magnitude of crustal extension in the southern Great Basin, *Geology* 10 (1982) 499–503.
- [4] N. Niemi, B. Wernicke, R. Brady, J. Saleeby, G. Dunne, Magnitude and timing of extreme continental extension, central Death Valley region, California, in: J. Slate (Ed.), *Proceedings of Conference on Status of Geologic Research and Mapping, Death Valley National Park, Open-File Rep.* (U. S. Geol. Surv.), vol. 99-0153, Geological Society of America, Denver, Colorado, 1999, pp. 33–35.
- [5] H. Fossen, A. Roernes, Properties of fault populations in the Gullfaks Field, northern North Sea, *J. Struct. Geol.* 18 (1996) 179–190.
- [6] G. Viejo, M. Laigle, C. Raneroc, Pre-Permian sedimentary basins in the North Sea: images from reprocessed and pre-stack depth migrated MONA LISA data, *Mar. Pet. Geol.* 19 (2002) 519–526.
- [7] G. Axen, B. Wernicke, M. Skelly, W. Taylor, Mesozoic and Cenozoic tectonics of the Sevier thrust belt in the Virgin River Valley area, southern Nevada, in: B. Wernicke (Ed.), *Basin and Range Extensional Tectonics Near the Latitude of Las Vegas, Nevada*, Mem.-Geol. Soc. Am., vol. 176, Geological Society of America, Boulder, Colorado, 1990, pp. 123–153.
- [8] E. Duebendorfer, A. Sewall, E. Smith, The Saddle Island detachment: an evolving shear zone in the Lake Mead area, Nevada, in: B. Wernicke (Ed.), *Basin and Range Extensional Tectonics Near the Latitude of Las Vegas, Nevada*, Mem.-Geol. Soc. Am., vol. 176, Geological Society of America, Boulder, Colorado, 1990, pp. 77–97.
- [9] K. Hodges, L. McKenna, M. Harding, Structural unroofing of the central Panamint Mountains, Death Valley region, southeastern California, in: B. Wernicke (Ed.), *Basin and Range Extensional Tectonics Near the Latitude of Las Vegas, Nevada*, Mem.-Geol. Soc. Am., vol. 176, Geological Society of America, Boulder, Colorado, 1990, pp. 377–388.
- [10] J. Spencer, S. Reynolds, Tectonics of mid-tertiary extension along a transect through west central Arizona, *Tectonics* 10 (1991) 1204–1221.
- [11] P. Gauthier, J.-P. Brun, Crustal-scale geometry and kinematics of late-orogenic extension in the central Aegean (Cyclades and Evvia Island), *Tectonophysics* 238 (1994) 399–424.
- [12] M. Forster, G. Lister, Detachment faults in the Aegean core complex of Ios, Cyclades, Greece, in: U. Ring, M. Brandon, G. Lister, S. Willett (Eds.), *Exhumation Processes: Normal Faulting, Ductile Flow and Erosion*, Spec. Publ.-Geol. Soc. Lond., vol. 154, 1999, pp. 305–323.
- [13] C. Burchfiel, R. Nakov, T. Tzankov, L. Royden, Cenozoic extension in Bulgaria and northern Greece: the northern part of the Aegean extensional regime, in: E. Bozkurt, J. Winchester, J. Piper (Eds.), *Tectonics and Magmatism in Turkey and the Surrounding Area*, Spec. Publ.-Geol. Soc. Lond., vol. 173, 2000, pp. 325–352.
- [14] K. Gessner, U. Ring, C. Johnson, R. Hetzel, C. Passchier, T. GÜngör, An active bivergent rolling-hinge detachment system: Central Menderes metamorphic core complex in western Turkey, *Geology* 29 (2001) 611–614.
- [15] P. Christiansen, D. Pollard, Nucleation, growth and structural development of mylonitic shear zones in granitic rock, *J. Struct. Geol.* 19 (1997) 1159–1172.
- [16] B. Wernicke, Theory of large-scale, uniform-sense normal simple shear of the continental lithosphere, *Can. J. Earth Sci.* 22 (1985) 108–125.
- [17] B. Wernicke, G. Axen, On the role of isostasy in the evolution of normal fault systems, *Geology* 16 (1988) 848–851.
- [18] H. Koyi, A. Skelton, Centrifuge modelling of the evolution of low-angle detachment faults from high-angle normal faults, *J. Struct. Geol.* 23 (2001) 1179–1185.
- [19] J.-P. Brun, D. Sokoutis, J. van den Driessche, Analogue modelling of detachment fault systems and core complexes, *Geology* 22 (1994) 319–322.
- [20] G. Mulugeta, W. Ghebreab, Modeling heterogeneous stretching during episodic or steady rifting of the continental lithosphere, *Geology* 29 (2001) 895–898.
- [21] G. Corti, M. Bonini, F. Innocenti, P. Manetti, G. Mulugeta, Centrifuge models simulating magma emplacement during oblique rifting, *J. Geodyn.* 31 (2001) 557–576.
- [22] J. Dunbar, D. Sawyer, How preexisting weaknesses control the style of continental breakup, *J. Geophys. Res.* 94 (1989) 7278–7292.
- [23] L. Moresi, H.-B. Mühlhaus, F. Dufour, Viscoelastic formulation for modelling of plate tectonics, in: H.-B. Mühlhaus, A. Dyskin, E. Pasternak (Eds.), *Bifurcation and Localization in Soils and Rocks*, Balkema, Rotterdam, 2001, pp. 337–344.
- [24] L. Moresi, F. Dufour, H.-B. Mühlhaus, A Lagrangian integration point finite element method for large deformation modeling of viscoelastic geomaterials, *J. Comput. Phys.* 184 (2003) 476–497.
- [25] L.N. Moresi, A. Lenardic, Three-dimensional mantle convection with continental crust: first-generation numerical simulations, *Earth Interact.* 3 (1999) 1–14.
- [26] H.-B. Mühlhaus, H. Sakaguchi, L. Moresi, N. Graham, Particle in cell and discrete element models for granular materials, in: C. Desai, T. Kundu, S. Harpalany, D. Contractor, J. Kemini (Eds.), *Computer Methods and Advances in Geomechanics*, Balkema, Rotterdam, 2001, pp. 511–518.
- [27] H.-B. Mühlhaus, L. Moresi, B. Hobbs, F. Dufour, Large amplitude folding in finely layered viscoelastic rock structures, *Pure Appl. Geophys.* 159 (2002) 2311–2333.
- [28] J. Byerlee, Brittle-ductile transition in rocks, *J. Geophys. Res.* 73 (1968) 4741–4750.
- [29] J. Suppe, *Principles of Structural Geology*, Prentice-Hall, New Jersey, 1985, 537 pp.
- [30] D. Frank-Kamenetskii, *Diffusion and Heat Transfer in Chemical Kinetics*, 2nd edition, Plenum Press, New York, 1969, 574 pp.
- [31] W. Brace, D. Kohlstedt, Limits on lithospheric stress imposed by laboratory experiments, *J. Geophys. Res.* 85 (1980) 6248–6252.
- [32] D. McKenzie, D. Fairhead, Estimates of the effective elastic thickness of the continental lithosphere from bouger and free air gravity anomalies, *J. Geophys. Res.* 102 (1997) 27523–27552.

- [33] M. Handy, S. Wissing, L. Streit, Frictional-viscous flow in mylonite with varied biminerale composition and its effect on lithospheric strength, *Tectonophysics* 303 (1999) 175–191.
- [34] P. Bird, X. Kong, Computer simulations of California tectonics confirm very low strength of major faults, *Geol. Soc. Amer. Bull.* 106 (1994) 159–174.
- [35] A. Lachenbruch, J. Sass, Heat flow and energetics of the San Andreas fault zone, *J. Geophys. Res.* 85 (1980) 6185–6222.
- [36] A. Lachenbruch, J. Sass, Heat flow from Cajon Pass, fault strength, and tectonic implications, *J. Geophys. Res.* 97 (1992) 4995–5015.
- [37] M. Zoback, W. Prescott, S. Krueger, Evidence for lower crustal ductile strain localization in southern New York, *Nature* 317 (1985) 705–707.
- [38] P. Saunders, K. Priestley, T. Taymaz, Variations in the crustal structure beneath western Turkey, *Geophys. J. Int.* 134 (1998) 373–389.
- [39] R. Hetzel, U. Ring, C. Akal, M. Trosch, Miocene NNE-directed extensional unroofing in the Menderes massif, south-western Turkey, *J. Geol. Soc. (Lond.)* 152 (1995) 639–654.
- [40] T. Parsons, J. McCarthy, G. Thompson, Very different response to extreme extension in the southern Basin and Range and Colorado Plateau transition, in: M. Erskine, J. Faulds, J. Bartley, P. Rowley (Eds.), *American Association of Petroleum Geologists Pacific Section Guidebook*, vol. 78, 2001, pp. 291–303.
- [41] L. Montési, M. Zuber, Spacing of faults at the scale of the lithosphere and localisation instability: 1. Theory, *J. Geophys. Res.* 108 (2003) 2110.
- [42] T. Bai, D. Pollard, Fracture spacing in layered rocks: a new explanation based on the stress transition, *J. Struct. Geol.* 22 (2000) 43–57.
- [43] C. Ebinger, N. Hayward, Soft plates and hot spots: views from afar, *J. Geophys. Res.* 101 (1996) 21859–21876.
- [44] F. Vening-Meinesz, Les grabens africains résultant de compression ou de tension dans la croûte terrestre, *Bull. Inst. R. Colon. Belge* 21 (1950) 539–552.
- [45] W. Buck, Modes of continental lithospheric extension, *J. Geophys. Res.* 96 (1991) 20161–20178.
- [46] V. Benes, P. Davy, Modes of continental lithospheric extension: experimental verification of strain localization processes, *Tectonophysics* 254 (1996) 169–187.
- [47] E. Hauser, T. Gephart, T. Latham, L. Bown, S. Kaufman, J. Oliver, I. Lucchitta, COCORP Arizona transect: strong crustal reflection data, *Geol. Soc. Amer. Bull.* 99 (1987) 833–844.
- [48] R. Scott, G. Lister, Detachment faults: evidence for a low-angle origin, *Geology* 20 (1992) 833–836.
- [49] R.F. Livaccari, J.W. Geissman, S.J. Reynolds, Large-magnitude extensional deformation in the South Mountains metamorphic core complex, Arizona: evaluation with paleomagnetism, *Geol. Soc. Amer. Bull.* 107 (1995) 877–894.
- [50] W. Buck, Flexural rotation of normal faults, *Tectonics* 7 (1988) 959–973.
- [51] S. Wills, W. Buck, Stress-field rotation and rooted detachment faults: a Coulomb failure analysis, *J. Geophys. Res.* 102 (1997) 20503–20514.
- [52] F. Horvath, Towards a mechanical model for the formation of the Pannonian Basin, in: S. Cloetingh, W. Sassi, F. Horvath (Eds.), *The Origin of Sedimentary Basins: Inferences from Quantitative Modelling and Basin Analysis*, Elsevier, Amsterdam, 1993, pp. 333–357.
- [53] L. Lavier, W. Buck, A. Poliakov, Factors controlling normal fault offset in an ideal brittle layer, *J. Geophys. Res.* 105 (2000) 23431–23442.
- [54] L. Lavier, W. Buck, Half graben versus large-offset low-angle normal fault: importance of keeping cool during normal faulting, *J. Geophys. Res.* 107 (2002), doi:10.1029/2001JB000513.
- [55] F. Pollitz, C. Wicks, W. Thatcher, Mantle flow beneath a continental strike-slip fault: postseismic deformation after the 1999 Hector Mine earthquake, *Science* 293 (2001) 1814–1818.
- [56] G. Chulick, W. Mooney, Seismic structure of the crust and uppermost mantle of North America and adjacent oceanic basins: a synthesis, *Bull. Seismol. Soc. Am.* 92 (2002) 2478–2492.